Continuous Reduced-Order Dynamic Model Based on Energy Balancing for Inductive Power Transfer Systems

Shi, Wenli; Dong, Jianning; Soeiro, Thiago B.; Deng, Junjun; Riekerk, Calvin; Bauer, Pavol

DOI
10.1109/TPEL.2022.3153846

Publication date
2022

Document Version
Final published version

Published in
IEEE Transactions on Power Electronics

Citation (APA)
Shi, W., Dong, J., Soeiro, T. B., Deng, J., Riekerk, C., & Bauer, P. (2022). Continuous Reduced-Order Dynamic Model Based on Energy Balancing for Inductive Power Transfer Systems. *IEEE Transactions on Power Electronics*, *37*(8), 9959-9971. Article 9721577. https://doi.org/10.1109/TPEL.2022.3153846

Continuous Reduced-Order Dynamic Model Based on Energy Balancing for Inductive Power Transfer Systems

Wenli Shi, *Graduate Student Member, IEEE*, Jianning Dong, *Member, IEEE*,
Thiago Batista Soeiro, *Senior Member, IEEE*, Junjun Deng, *Member, IEEE*,
Calvin Riekerk, *Graduate Student Member, IEEE*, and Pavol Bauer, *Senior Member, IEEE*

***Abstract*—Resonant circuits are commonly used in inductive power transfer (IPT) systems for the charging of electric vehicles because of the high power efficiency. Transient behaviors of the resonant circuits, which play a significant role in the design and analysis of IPT systems, are cumbersome to model analytically because of the high-order. This article develops a reduced-order continuous dynamic model based on the energy interactions among the resonant tanks. By applying the proposed energy balancing method (EBM), the order of the dynamic model is reduced to half of the number of the passive components in the resonant circuits. To show the accuracy of the EBM, the dynamics of a series–series (SS) compensated IPT system are modeled using Laplace phasor transformation (LPT) and EBM separately and the results are compared. The order of the EBM is found to be one-fourth of that of the LPT method. The sensitivity of the EBM to the switching frequency is discussed when the zero voltage switching turn-ON operation is attained. Besides, to prove the advantage of reducing the order of the dynamic model, model predictive controls (MPCs) based on EBM and LPT are developed. The transient performances of the MPC controllers are simulated and the control inputs are applied to an experimental setup. Finally, experiments are conducted to verify the accuracy of the proposed EBM under zero and nonzero conditions and the effectiveness of the developed MPC controller.**

***Index Terms*—Electric vehicles (EVs), inductive power transfer (IPT), model predictive control (MPC), reduced-order dynamic model, resonant circuits.**

I. INTRODUCTION

THE inductive power transfer (IPT) technology is under rapid development for dynamic charging of electric vehicles (EVs) [1]–[6]. In dynamic IPT (DIPT) systems, several transmitter pads (Tx) are mounted under the road, allowing EVs to pick up power while they are moving. Thus, the drive range of EVs can be extended. One of the main challenges of the DIPT application is the common variation of the mutual coupling between Tx and the EV receiver pad (Rx) due to the misalignment caused by the EV movement, i.e., as the EV moves toward the perfect alignment condition, the mutual coupling changes from the minimum to the maximum [7]–[9]. Consequently, the operation state of the power electronic converters will continuously change and the power picked up by the EV battery charger may fluctuate. Also, the start-up transients of the IPT systems should be regulated to avoid any overcurrent or voltage problems [10], [11]. Moreover, the disturbances in the dc source may lead to an unstable output of the IPT systems. To address these dynamic challenges, it is essential to have a dynamic model for the design of IPT systems.

The basic schematic of an IPT system is presented in Fig. 1 [12]. This circuit implements a power factor correction circuit for compliance with integration guidelines to the public ac grid (the ac–dc front-end), an isolated resonant-based dc–dc converter comprising an H-bridge inverter cascaded to a series–series (SS) capacitive compensation circuit forming a two-stage equivalent series resonant tank with the transmitter and receiver coils and a rectifying stage (the back-end ac–dc converter). Finally, a nonisolated dc–dc converter can be used to control the charging profile across the battery of the vehicle. This final circuit can be controlled so that the battery and nonisolated dc–dc converter will behave as a controllable equivalent resistive load for the isolated dc–dc resonant converter [13]. Due to the presence of switching converters, the instantaneous model of the IPT system is discontinuous and time-variant. To study a specific design, the instantaneous model can be processed numerically to evaluate its dynamic characteristics [14]. However, the instantaneous model offers limited insights into the design of the feedback controller and the optimization of the resonant circuit components. To overcome the discontinuity and time-variance of the instantaneous model and to derive analytic solutions, the oscillating state variables can be transformed into slowly varying variables based on the short-time Fourier transform. Existing studies report dynamic modeling methods, including the state-space averaging (SSA), generalized SSA (GSSA) [15],

---

Manuscript received June 22, 2021; revised October 28, 2021 and December 27, 2021; accepted February 19, 2022. Date of publication February 25, 2022; date of current version April 28, 2022. The work was supported by China Scholarship Council under Grant 201806030152. Recommended for publication by Associate Editor O.C. Onar. *(Corresponding author: Jianning Dong.)*

Wenli Shi, Jianning Dong, Calvin Riekerk, and Pavol Bauer are with the Delft University of Technology, 2600 AA Delft, The Netherlands (e-mail: w.shi-3@tudelft.nl; j.dong-4@tudelft.nl; c.riekerk@tudelft.nl; p.bauer@tudelft.nl).

Thiago Batista Soeiro is with European Space Agency, 2200 AG Noordwijk, The Netherlands (e-mail: Thiago.BatistaSoeiro@esa.int).

Junjun Deng is with the Beijing Institute of Technology, Beijing 100811, China (e-mail: dengjunjun@bit.edu.cn).

Color versions of one or more figures in this article are available at https://doi.org/10.1109/TPEL.2022.3153846.

Digital Object Identifier 10.1109/TPEL.2022.3153846

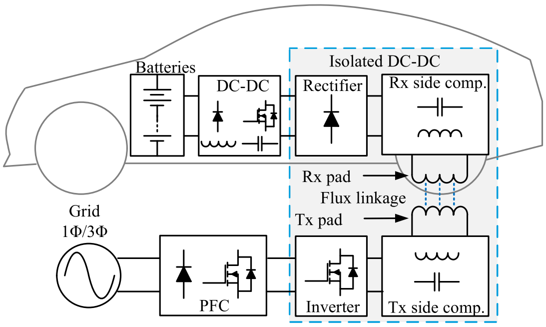

Fig. 1. Core schematic of an IPT system.

[16], Laplace phasor transformation (LPT) [17]–[19], extended describing function (EDF) [20], and coupled model theory (CMT) [21], [22].

The SSA method is not applicable for IPT systems since the fundamental harmonic components of state variables cannot be neglected [23]. The GSSA method is based on a time-dependent Fourier series representation for a sliding window of state variables. Depending on the accuracy of the model, the oscillating state variables can be replaced by their Fourier coefficients in the exponential form at different harmonic orders. Thanks to the property of the resonant circuit, the fundamental harmonics approximation (FHA) can usually deliver the accurate analysis of the IPT system performances. When FHA is applied to the GSSA model, each oscillating state variable is represented by a complex variable; thus, the order of the ac circuit is doubled.

The EDF method is based on the Fourier transform, where the oscillating state variables are expressed in trigonometric form instead of exponential form. Thus, there is no complex terms in the final state-space model, while the order of the ac circuit is also doubled. In [20], the SS capacitive compensated IPT system with an output filter capacitor is described as a ninth-order state-space model.

In the LPT method, the oscillating state variables are represented by a phasor, whose amplitude and phase are derived from the fundamental coefficients of the oscillating state variables. Therefore, the state-space models using GSSA and LPT are essentially the same. The advantage of the LPT method is that the time-domain model can be transformed into a phasor-domain model, where conventional circuit analysis techniques, such as Kirchhoff's voltage and current laws, and Thevenin's and Norton's theorems, can be easily applied [18]. By using the LPT method, it is possible to reduce the order of the state-space model through circuit analysis [19]. However, since a phasor contains two time varying variables, the LPT method still increases the order of the final state-space model.

The CMT method models the *LC* resonant tank from the energy point of view. This method is first applied to the IPT system in [24], and it has been shown that it is effective in analyzing the efficiency of an SS compensated IPT system [24], [25]. In [22], the CMT method is first combined with the SSA to model the dynamic characteristics of an IPT system using SS compensation. In an *LC* resonant tank, the oscillating current through the inductor and the voltage across the capacitor can be replaced by the energy magnitude and phase, which are two slowly varying real variables. Therefore, the order of the state-space model derived from the CMT method is equal to that of the instantaneous state-space model. A similar method is reported in [26], where the secondary side circuit using parallel compensation is transformed into a dc circuit preserving the energy balance. However, the primary side circuit is not addressed.

The high-order of dynamic models makes it hard for researchers to gain insights on the transient behaviors of an IPT system [19]. Besides, it obstructs the applications of control strategies, where the analytical dynamic model is required. The model predictive control (MPC), a discrete optimal control strategy, applies the system analytic model to periodically predict its future behaviors. The MPC is insensitive to disturbances [5] and can provide fast dynamic response [27]. Since the continuous dynamic model of the IPT systems is complex, the MPC is mainly designed based on the static model of the ac-link to control the H-bridge converters [28] or based on the dynamic model of the dc–dc converters to control the secondary side converter. Without the dynamic model of the ac-link, these control methods cannot improve the transient behaviors inside the ac-link, which may cause a large overshoot.

In summary, the existing dynamic modeling methods can only deliver continuous dynamic models whose orders are equal to or higher than the number of the passive components. To simplify the transient analysis and facilitate the application of control strategies relying on the analytical system model, it becomes essential to describe IPT systems using a continuous time-invariant and low-order state-space model. Therefore, this article proposes a new dynamic modeling approach—an energy balancing method (EBM) based on the energy interactions between the resonant tanks for loosely coupled IPT systems using SS capacitive compensation. The order of the dynamic model using EBM is half the number of the passive components in the resonant circuits. An MPC controller is developed to prove the advantage of the proposed EBM.

The main contributions of this article include the following.

1) A new dynamic modeling method based on the balance of energy is proposed. The proposed EBM can significantly reduce the dynamic model order of the resonant circuits. This is an important factor to facilitate the implementation of control strategies relying on the system analytical models, such as MPC.
2) The accuracy of the proposed EBM in predicting the transient response is benchmarked with the LPT method when the system starts from zero and nonzero conditions.
3) The transient response of the winding current phase angle is discussed and found to be minimal when the IPT system operates near the resonance frequency.
4) An MPC strategy based on the proposed EBM is developed and experimentally verified. This proves that the EBM is well suited for IPT systems taking the advantage of the MPC technique.

The rest of this article is organized as follows. In Section II, the derivation of the EBM for various resonant tanks is presented. In Section III, the proposed EBM is compared with the LPT method while analyzing the transient behavior of an SS compensated

TABLE I
CIRCUIT PARAMETERS OF THE SS COMPENSATED IPT SYSTEM

Variables	Unit	Case A Value	Case B Value
L_1	μH	301.65	292.77
L_2	μH	202.17	199.18
M	μH	15.69	17.21
C_1	nF	11.70	11.69
C_2	nF	17.12	17.11
C_{fo}	μF	100	100
R_1	Ω	0.1	0.1
R_2	Ω	0.5	0.7
R_L	Ω	10	8.6
$\omega_{r,1}$	kHz	84.7	86.0
$\omega_{r,2}$	kHz	85.5	86.2
ω_s	kHz	85.6	86.3

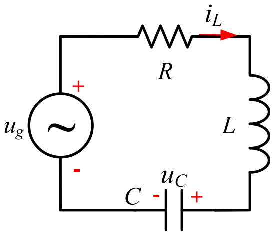

Fig. 2. *LC* resonant tank.

IPT system. It is shown that the order of the resonant circuits dynamic model using the EBM is one-fourth that of the resulting model derived with the LPT. The sensitivity of the EBM to the switching frequency of the inverter is also discussed. In Section IV, the MPC controller based on the EBM and LPT methods is developed and their transient behaviors are compared. In Section V, experiments are conducted to verify the accuracy of the dynamic models using EBM and the effectiveness of the developed MPC controller. Finally, Section VI concludes this article.

II. TRANSIENT BEHAVIORS OF RESONANT TANKS

In this section, the energy balancing model of the *LC* and coupled *LC* resonant tanks is derived.

A. *Energy of an LC Resonant Tank*

The *LC* resonant tank is presented in Fig. 2. The resonant frequency of the *LC* tank ω_s is

$$\omega_s = \frac{1}{\sqrt{LC}}. \tag{1}$$

The *LC* circuit operating under resonance can be modeled as

$$\begin{bmatrix} i'_L \\ u'_C \end{bmatrix} = \begin{bmatrix} -\frac{R}{L} & -\frac{1}{L} \\ \frac{1}{C} & 0 \end{bmatrix} \begin{bmatrix} i_L \\ u_C \end{bmatrix} + \begin{bmatrix} \frac{1}{L} \\ 0 \end{bmatrix} u_g \tag{2}$$

where the prime in the symbols represents the time differential. To investigate the step response of the *LC* tank, the voltage source $u_g = U_g \cos(\omega t)$ is applied at t_0, where U_g is constant. Provided $R < 2\omega_s L$, the state-space model in (2) can be solved as

$$i_L = U_g \frac{1}{R} \cos(\omega_s t) + e^{-\frac{R}{2L}t} \left(\frac{i_L(0)R - U_g}{R} \cos\left(\frac{H}{2L}t\right) - \frac{i_L(0)R + 2u_C(0) - U_g}{H} \sin\left(\frac{H}{2L}t\right) \right) \tag{3}$$

$$u_C = U_g \frac{\omega_s L}{R} \sin(\omega_s t) + e^{-\frac{R}{2L}t} \left(u_C(0) \cos\left(\frac{H}{2L}t\right) + \frac{2\omega_s{}^2 L^2 (i_L(0)R - U_g) + u_C(0)R^2}{RH} \sin\left(\frac{H}{2L}t\right) \right) \tag{4}$$

$$H = \sqrt{4\omega_s{}^2 L^2 - R^2}. \tag{5}$$

As shown in (3) and (4), the decay rate of the state variables is $\tau_{LC} = -\frac{R}{2L}$. By increasing R, the *LC* resonant tank can rapidly reach the steady state, and the transients can be mostly neglected. Given $R = \omega_s L$, for example, the transient components in (3) and (4) decay to below 5% within one switching cycle. In contrast, the transient response of the *LC* tank deteriorates as R decreases. When $R << \omega_s L$, $H \approx 2\omega_s L$, and the solutions under zero conditions become

$$\begin{cases} i_L \approx U_g \frac{1}{R} \cos(\omega_s t)(1 - e^{-\frac{R}{2L}t}) \\ u_C \approx U_g \frac{\omega_s L}{R} \sin(\omega_s t)(1 - e^{-\frac{R}{2L}t}). \end{cases} \tag{6}$$

The total energy in the *LC* resonant tank W_{LC} is

$$W_{LC} = \frac{1}{2} L i_L^2 + \frac{1}{2} C u_C^2. \tag{7}$$

By substituting (6)–(7), the time-domain solution of W_{LC} under resonance can be obtained

$$W_{LC} = \frac{L U_g^2}{2R^2} (1 + e^{-\frac{R}{L}} - 2e^{-\frac{R}{2L}}). \tag{8}$$

As per in (8), W_{LC} is a slow-varying positive variable, which does not contain any oscillating component. Meanwhile, (6) proves that i_L peaks when u_C becomes zero, which means the total energy of the *LC* tank is stored in the inductor as i_L reaches the peak, and vice versa. Therefore, the amplitude of i_L and u_C, and I_L and U_C can be expressed as (9). By introducing (9), I_L and U_C can be calculated by solving W_{LC} instead of i_L and u_C, which are cumbersome to solve due to their oscillating nature

$$I_L = \sqrt{\frac{2W_{LC}}{L}}, U_C = \sqrt{\frac{2W_{LC}}{C}}. \tag{9}$$

B. *Energy Balancing Model for an LC Resonant Tank*

The energy injected from the voltage source will either increase W_{LC} or be consumed by the load. The phase angle between u_g and i_L is negligible as per (6). Thus, based on the balance of energy, the *LC* resonant tank can be modeled as

$$W'_{LC} = L I_L I'_L = \frac{1}{2} U_g I_L - \frac{1}{2} I_L^2 R. \tag{10}$$

Based on (10), the dynamic model of the *LC* resonant tank using the EBM can be derived

$$I'_L = -\frac{R}{2L} I_L + \frac{1}{2L} U_g. \tag{11}$$

U_C can be obtained from (9). Compared with the dynamic model in (2), the model applying the EBM in (11) applies the amplitude of the oscillating variable to model the *LC* resonant

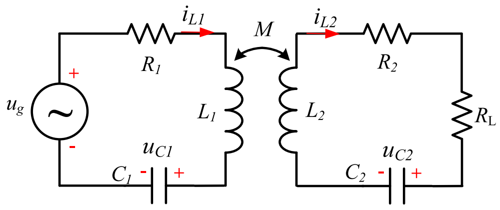

Fig. 3. Two coupled *LC* resonant tanks.

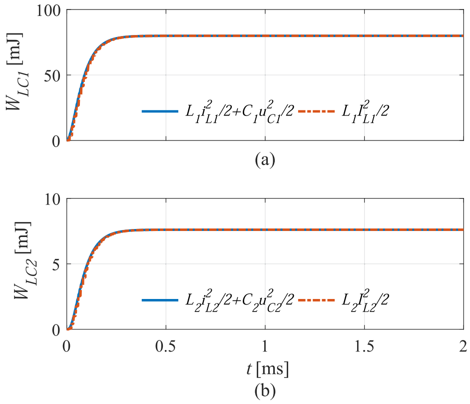

Fig. 4. Total energy stored in the *LC* resonant tanks during transients, (a) LC1 and (b) LC2, where $L_1 = 63.35\ \mu$H, $L_2 = 43.53\ \mu$H, $M = 6.1\ \mu$H, $R_1 = 0.2\ \Omega$, $R_2 = 0.3\ \Omega$, and $R_L = 20\ \Omega$.

tank instead of the oscillating variables themselves. As a result, the order of the dynamic model is reduced by half and the state variables are real-value.

C. Energy Balancing Model for Two Coupled LC Resonant Tanks

The EBM can also be applied to model two coupled *LC* resonant tanks, L_1C_1 (as LC1) and L_2C_2 (as LC2), as shown in Fig. 3. Fig. 4 presents agreement between the total energy calculated based on the instantaneous winding current and the capacitor voltage and the amplitude of the winding current. This means the phase angle between i_{L1} (i_{L2}) and u_{c1} (u_{c2}) maintains to be $\frac{\pi}{2}$ as in (6). Assuming that the resonant frequency of both resonant tanks is equal to ω_s, the energy of the resonant tanks can be expressed as

$$\begin{cases} W_{LC1} = \frac{1}{2}L_1I_{L1}^2 \\ W_{LC2} = \frac{1}{2}L_2I_{L2}^2. \end{cases} \tag{12}$$

In EV charging applications employing IPT systems, the presence of air gap between charging pads causes the coupling coefficient to be relatively low. Thus, the phase angle between u_g and i_{L1} can be neglected as proved by (6). The energy interaction between LC1 and LC2 can be calculated with

$$W'_{LC1} = L_1I_{L1}I'_{L1} = \frac{1}{2}U_gI_{L1} - \frac{1}{2}I_{L1}^2R_1 - \frac{1}{2}\omega_sMI_{L1}I_{L2} \tag{13}$$

$$W'_{LC2} = L_2I_{L2}I'_{L2} = \frac{1}{2}\omega_sMI_{L1}I_{L2} - \frac{1}{2}I_{L2}^2(R_L + R_2) \tag{14}$$

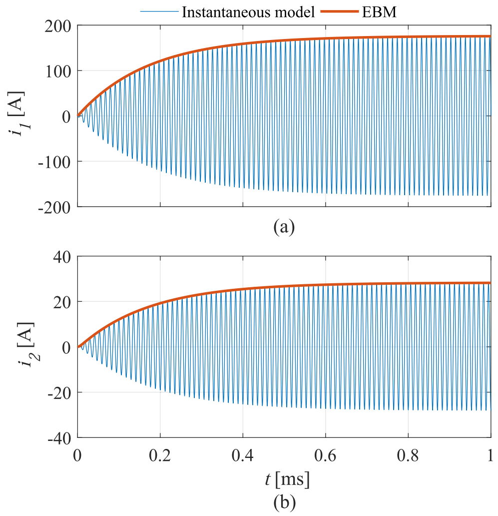

Fig. 5. Time-domain solutions of two coupled *LC* resonant tanks from the instantaneous model and EBM, where $U_g = 100$V and the circuit parameters are the same as Fig. 4.

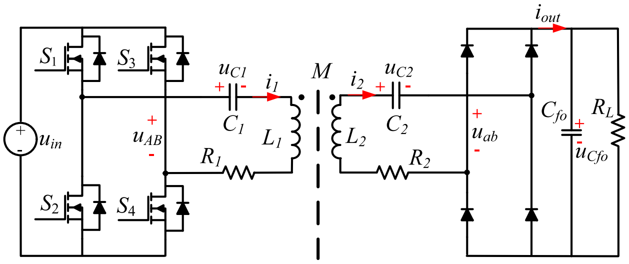

Fig. 6. Schematic of the SS compensated IPT system.

where I_{L1} and I_{L2} are the amplitudes of i_{L1} and i_{L2}, respectively. Based on (13) and (14), the dynamic model using EBM can be obtained as

$$\begin{bmatrix} I'_{L1} \\ I'_{L2} \end{bmatrix} = \begin{bmatrix} -\frac{R_1}{2L_1} & -\frac{\omega_sM}{2L_1} \\ \frac{\omega_sM}{2L_2} & -\frac{(R_2+R_L)}{2L_2} \end{bmatrix} \begin{bmatrix} I_{L1} \\ I_{L2} \end{bmatrix} + \begin{bmatrix} \frac{1}{2L_1} \\ 0 \end{bmatrix} U_g. \tag{15}$$

The solutions from the instantaneous model and EBM are presented in Fig. 5, where the amplitude of waveforms obtained from EBM match the envelopes of waveforms from the instantaneous model.

III. APPLYING EBM TO THE SS COMPENSATED IPT SYSTEM

This section presents the modeling procedure of an SS compensated IPT system using the developed EBM. To highlight the advantage of EBM in reducing the dynamic model order of the IPT system, the dynamic model using LPT is also derived for comparison purpose.

A. SS Compensated IPT System

The schematic of the studied IPT system is presented in Fig. 6. The main power stage consists of a dc voltage source, an H-bridge inverter, a primary and secondary resonant circuit, an H-bridge diode rectifier, and an equivalent modeled resistive load with a capacitive filter in parallel. The dc voltage u_{in} is converted into the ac voltage u_{AB} by the inverter. u_{AB} is a square waveform with the fundamental harmonic angular frequency as ω_s. The resonant circuits on both sides include the inductances L_1 and L_2, the capacitances C_1 and C_2, and the equivalent parasitic series ac resistances R_1 and R_2. The mutual inductance between the Tx and Rx is M. The voltages across C_1 and C_2 are u_{C1} and u_{C2}, respectively. The rectifier converts i_2 into the dc current i_{out}, which feeds power to the filter capacitor C_{fo} and equivalent resistive load R_L. To reduce the voltage ripple across the load voltage u_{Cfo}, a large filter capacitor C_{fo} is connected in parallel with R_L.

The SS compensation is one of the basic compensation topologies that uses a single capacitor in each coil side to form the resonant circuits in the IPT systems. The ac-link of the SS compensated IPT system is of fourth order, so its instantaneous state-space model will also be of the same order. To deal with the discontinuity of the instantaneous model, the state variables are replaced by their Fourier series coefficient. As the resonant circuits operate as a low-pass filter, FHA can deliver the accurate estimation of the system performances.

B. Dynamic Model Using LPT

The inverter and rectifier stages can be analyzed by using the equivalent turns ratio [17]. Assuming that the dead time of the H-bridge inverter PWM signal is negligible, the equivalent turns ratio of the inverter s_1 and rectifier s_2 can be expressed as

$$s_1 = \operatorname{sgn}[\cos(\omega t)], u_{AB} = s_1 u_{in} \tag{16}$$

$$s_2 = \operatorname{sgn}[i_2], u_{ab} = s_2 u_{Cfo}, i_{out} = s_2 i_2. \tag{17}$$

By using the instantaneous variables, the fifth-order instantaneous state-space model of the SS compensated IPT system is given by

$$\left\{\begin{aligned} \begin{bmatrix} i_1' \\ u_{C1}' \\ i_2' \\ u_{C2}' \\ u_{Cfo}' \end{bmatrix} &= \mathbf{A_{p1}} \begin{bmatrix} i_1 \\ u_{C1} \\ i_2 \\ u_{C2} \\ u_{Cfo} \end{bmatrix} + \mathbf{B_{p1}} s_1 u_{in} \\ \mathbf{A_{p1}} &= \begin{bmatrix} -\frac{L_2 R_1}{F} & -\frac{L_2}{F} & \frac{M R_2}{F} & \frac{M}{F} & -\frac{M s_2}{F} \\ \frac{1}{C_1} & 0 & 0 & 0 & 0 \\ \frac{M R_1}{F} & \frac{M}{F} & -\frac{L_1 R_2}{F} & -\frac{L_1}{F} & \frac{L_1 s_2}{F} \\ 0 & 0 & \frac{1}{C_2} & 0 & 0 \\ 0 & 0 & -\frac{s_2}{C_{fo}} & 0 & -\frac{1}{R_L C_{fo}} \end{bmatrix} \\ \mathbf{B_{p1}} &= \begin{bmatrix} \frac{L_2}{F} \\ 0 \\ -\frac{M}{F} \\ 0 \\ 0 \end{bmatrix} \\ F &= L_1 L_2 - M^2. \end{aligned}\right. \tag{18}$$

In the phasor dynamic model, U_{in}, U_{Cfo}, and I_{out} are the averaged values of the variables u_{in}, u_{Cfo}, and i_{out}, $\dot{I}_1$, $\dot{I}_2$, $\dot{U_{C1}}$, and $\dot{U_{C2}}$ are the dynamic phasors of the ac variables i_1, i_2, u_{C1}, and u_{C2}, $\dot{S}_1$ and $\dot{S}_2$ are the complex turns ratio of the inverter and the rectifier, respectively. To regulate the power flow, the phase shift control is used to control the inverter output voltage by adjusting its conduction angle $\theta \in [0, \pi]$ [16]. Taking the phase angle of $\dot{U_{AB}}$ as reference, the complex turns ratio $\dot{S}_1$ and $\dot{S}_2$ can be expressed as

$$\dot{S}_1 = \frac{2\sqrt{2}}{\pi} e^{j0} \sin\frac{\theta}{2}, \dot{U_{AB}} = \dot{S}_1 U_{\text{in}} \tag{19}$$

$$\dot{S}_2 = \frac{2\sqrt{2}}{\pi} e^{j[\arg(\dot{I}_2)]}, \dot{U_{ab}} = \dot{S}_2 U_{Cfo}, I_{\text{out}} = Re[\dot{S}_2^* \dot{I}_2]. \tag{20}$$

Since the phase angle of $\dot{S}_2$ is the same as that of $\dot{I}_2$, I_{out} can also be calculated as $I_{\text{out}} = |\dot{S}_2| e^{-j[\arg(\dot{I}_2)]} \dot{I}_2$.

The relation between the instantaneous variable x and its dynamic phasor $\dot{X}$ is given as

$$x = Re[\sqrt{2}\dot{X} e^{j\omega_s t}]. \tag{21}$$

Based on (19)–(21), (18) can be rewritten as

$$\left\{\begin{aligned} \begin{bmatrix} (\dot{I}_1{}' + j\omega_s \dot{I}_1) e^{j\omega_s t} \\ (\dot{U_{C1}}{}' + j\omega_s \dot{U_{C1}}) e^{j\omega_s t} \\ (\dot{I}_2{}' + j\omega_s \dot{I}_2) e^{j\omega_s t} \\ (\dot{U_{C2}}{}' + j\omega_s \dot{U_{C2}}) e^{j\omega_s t} \\ U_{Cfo}' e^{j\omega_s t} \end{bmatrix} &= \mathbf{A_{p2}} \begin{bmatrix} \dot{I}_1 e^{j\omega_s t} \\ \dot{U_{C1}} e^{j\omega_s t} \\ \dot{I}_2 e^{j\omega_s t} \\ \dot{U_{C2}} e^{j\omega_s t} \\ U_{Cfo} e^{j\omega_s t} \end{bmatrix} \\ &\quad + \mathbf{B_{p1}} \left[\dot{S}_1 e^{j\omega_s t} U_{\text{in}}\right] \\ \mathbf{A_{p2}} &= \begin{bmatrix} -\frac{L_2 R_1}{F} & -\frac{L_2}{F} & \frac{M R_2}{F} & \frac{M}{F} & -\frac{M \dot{S}_2}{F} \\ \frac{1}{C_1} & 0 & 0 & 0 & 0 \\ \frac{M R_1}{F} & \frac{M}{F} & -\frac{L_1 R_2}{F} & -\frac{L_1}{F} & \frac{L_1 \dot{S}_2}{F} \\ 0 & 0 & \frac{1}{C_2} & 0 & 0 \\ 0 & 0 & \frac{\left|\dot{S}_2\right| e^{-jarg[\dot{I}_2]}}{-C_{fo}} & 0 & -\frac{1}{R_L C_{fo}} \end{bmatrix} \end{aligned}\right. \tag{22}$$

$$\left\{\begin{aligned} \begin{bmatrix} \dot{I}_1{}' \\ \dot{U_{C1}}{}' \\ \dot{I}_2{}' \\ \dot{U_{C2}}{}' \\ U_{Cfo}' \end{bmatrix} &= \mathbf{A_{p3}} \begin{bmatrix} \dot{I}_1 \\ \dot{U_{C1}} \\ \dot{I}_2 \\ \dot{U_{C2}} \\ U_{Cfo} \end{bmatrix} + \mathbf{B_{p1}} \left[\dot{S}_1 U_{in}\right] \\ \mathbf{A_{p3}} &= \mathbf{A_{p2}} - j\omega_s \begin{bmatrix} \mathbf{I_{4\times4}} & \\ & 0 \end{bmatrix}. \end{aligned}\right. \tag{23}$$

By eliminating the term $e^{j\omega_s t}$ on both sides of (22), the fifth-order complex phasor dynamic model of the SS compensated IPT system is obtained in (23).

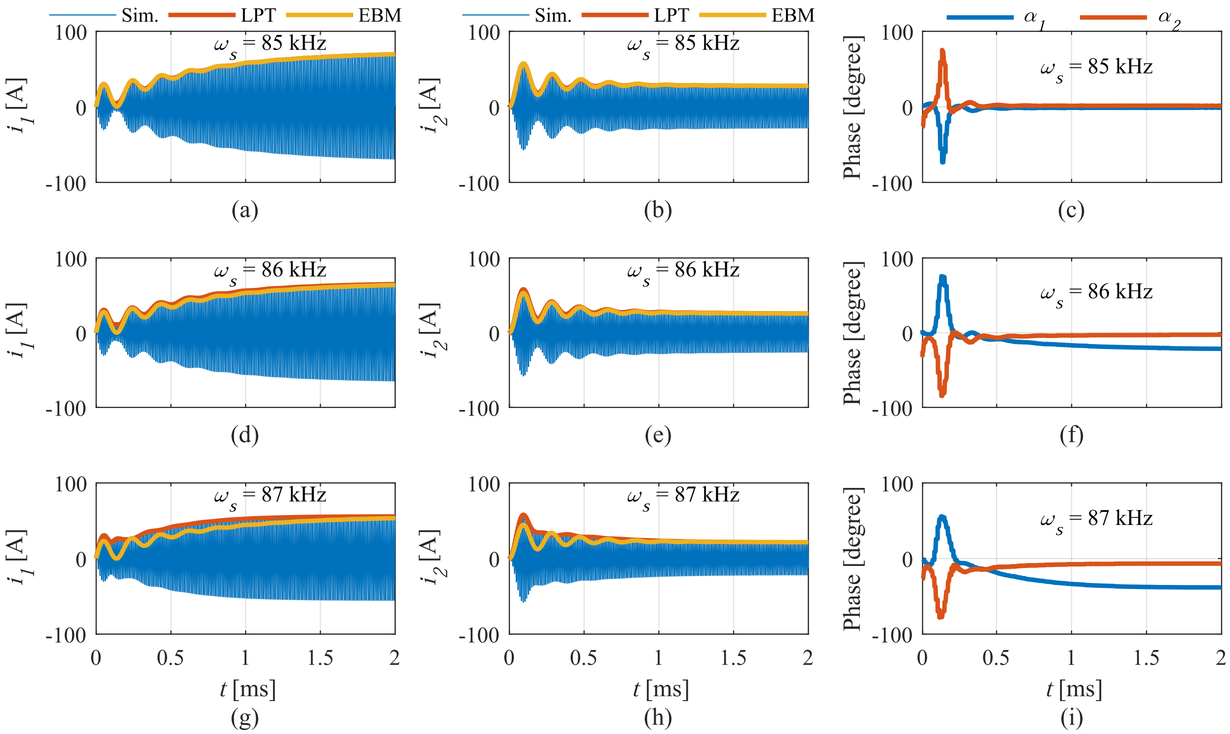

Fig. 7. Comparison between dynamic models using EBM and circuit simulations, where $u_{in} = 100$ V, $\omega_r = 85$ kHz, and $C_{fo} = 80$ μF, and the rest of the circuit parameters are the same as Fig. 4.

To derive the solutions of the dynamic phasor variables, the ninth-order real-valued dynamic model can be expressed as

$$\begin{cases} \mathbf{x_{LPT}} = [\dot{I}_{1,r}, \dot{U}_{C1,r}, \dot{I}_{2,r}, \dot{U}_{C2,r}, \\ \qquad \dot{I}_{1,i}, \dot{U}_{C1,i}, \dot{I}_{2,i}, \dot{U}_{C2,i}, U_{Cfo}]^T \\ \mathbf{x'_{LPT}} = \mathbf{A_{p4}} \mathbf{x_{LPT}} + \mathbf{B_{p2}} \begin{bmatrix} \dot{S}_{1,r} U_{in} \\ \dot{S}_{1,i} U_{in} \end{bmatrix} \\ \mathbf{B_{p2}} = \begin{bmatrix} \frac{L_2}{F} & 0 & -\frac{M}{F} & 0 & 0 & 0 & 0 & 0 & 0 \\ 0 & 0 & 0 & 0 & \frac{L_2}{F} & 0 & -\frac{M}{F} & 0 & 0 \end{bmatrix}^T \end{cases} \tag{24}$$

where $\mathbf{A_{p4}}$ is written in (27) shown at the bottom of the next page. In the transient state, the phase of $\dot{I}_2$ changes. $\dot{S}_{2,r}$, which is in phase with $\dot{I}_2$, becomes a time-varying variable. Therefore, the phasor dynamic model in (24) is still time-varying.

C. Dynamic Model Using EBM

In the EBM, the state variables are the fundamental harmonics amplitude of the oscillating instantaneous variables. I_1, I_2, U_{AB}, and U_{ab} are the amplitudes of i_1, i_2, u_{AB}, and u_{ab} at the resonant angular frequency ω_s. The equivalent turns ratios of the inverter S_1 and rectifier S_2 can be expressed in (27) and (28). The resonant frequency of the resonant circuit ω_r is assumed equal to ω_s. The output filter capacitor C_{fo} can be modeled by (25). The energy balance of the secondary resonant circuits can be expressed as (26). Based on (15), (25), and (26), the EBM dynamic model of the SS compensated IPT system is obtained in (30)

$$U'_{Cfo} = \frac{S_2 I_2}{2C_{fo}} - \frac{U_{Cfo}}{C_{fo} R_L} \tag{25}$$

$$L_2 I'_2 = \frac{\omega_s M I_1}{2} - \frac{R_2 I_2}{2} - \frac{S_2 U_{Cfo}}{2}. \tag{26}$$

D. Sensitivity of EBM When $\omega_s \neq \omega_r$

The developed EBM method is based on the assumption that ω_r is equal to ω_s. However, in real practice, ω_s might be tuned to make the input impedance of the resonant circuit slightly inductive, such that the zero voltage switching (ZVS) operation can be achieved in the inverter [29]. In the SS compensated IPT system, ω_s should be slightly larger than ω_r when the system works in nonbifurcation region [30]. Therefore, the sensitivity of the proposed EBM is discussed when $\omega_s \neq \omega_r$.

For the phase angle α_1 that represents the lagging of the waveform of i_1 in relation to u_{AB}, the average power injected into the primary resonant circuit becomes $\frac{1}{2} I_1 U_{AB} \cos(\alpha_1)$. Similarly, the power transferred to the secondary side is $\frac{1}{2} \omega M I_1 I_2 \cos(\alpha_2)$, where α_2 is the phase angle between i_2 and the secondary induced voltage. The revised dynamic model using EBM can be obtained as (31). The predicted results from EBM and LPT are compared with circuit simulations as shown in Fig. 7.

In Fig. 7(c) and (f), the transient behaviors of α_1 and α_2 are presented. Both α_1 and α_2 exhibit rapid transient responses, which last less than 0.25 ms when ω_s is below 86 kHz. Besides, their absolute values are mostly below 20°. This means that the primary and secondary resonant circuits are operating close to the resonance and (9) is still acceptably accurate. Consequently, it is reasonable for EBM to simplify the dynamic model by assuming that α_1 and α_2 remain at their steady states throughout the transients when ω_s is below 86 kHz. In Fig. 7(a) and (b), where $\omega_s = \omega_r$, the predicted results from the EBM and LPT match the simulated waveforms well. The transient and steady states are both accurately evaluated. When $\omega_s = 86$kHz, the steady state value of α_1 is around 20°, which can ensure ZVS operation of the inverter. As shown in Fig. 7(d) and (e), the predicted curves from the EBM and LPT both slightly deviate from the envelope of the simulated waveforms, while the estimation of the transient time and steady state values is still accurate.

However, as ω_s becomes larger than 87 kHz, as shown in Fig. 7(i), the transient time of α_1 and α_2 increases. Although the absolute value of α_2 maintains less than 9° over a large region, the steady state absolute value of α_1 is around 37°. This proves that the primary resonant circuits drift away from the resonance operation, and thus, (9) and the EBM become inaccurate. As presented in Fig. 7(g) and (h), the curves from the LPT match the simulated waveforms at the beginning of the transients, while fluctuating around the envelope of the waveforms with a small error. By contrast, the EBM constantly underestimates the amplitude of the waveforms during transient.

The power flow of IPT systems is commonly regulated via a natural resonant frequency tracking method that will tune the inverter operating frequency to an equivalent fixed-frequency control strategies, particularly because of the nonlinear relation of the output power to ω_s. Besides, by applying an equivalent fixed-frequency control strategy [5], [31], [32], the resonant circuit can operate at its natural optimum efficiency with minimum switching losses in the full-bridge inverter [33]. Indeed, it is normal for high-efficiency IPT systems employing optimal load matching that ω_s is tuned for the ZVS turn-ON operation of the H-bridge inverter and is close to the resonant frequency of the IPT systems. Therefore, the EBM is suitable to model IPT systems oriented for EV charging applications.

$$S_1 = \frac{4}{\pi}\sin\frac{\theta}{2}, U_{AB} = S_1 U_{\text{in}} \tag{28}$$

$$S_2 = \frac{4}{\pi}, U_{ab} = S_2 U_{Cfo}, I_{\text{out}} = \frac{1}{2} S_2 I_2 \tag{29}$$

$$\begin{cases} \mathbf{x_{EBM}} = & [I_1, I_2, U_{Cfo}]^T \\ \mathbf{x_{EBM}}' = & \mathbf{A_{e1}} \mathbf{x_{EBM}} + \mathbf{B_{e1}} S_1 U_{\text{in}} \\ \mathbf{A_{e1}} = & \begin{bmatrix} -\frac{R_1}{2L_1} & -\frac{\omega_s M}{2L_1} & 0 \\ \frac{\omega_s M}{2L_2} & -\frac{R_2}{2L_2} & -\frac{S_2}{2L_2} \\ 0 & \frac{S_2}{2C_{fo}} & -\frac{1}{C_{fo} R_L} \end{bmatrix} \\ \mathbf{B_{e1}} = & \begin{bmatrix} \frac{1}{2L_1} \\ 0 \\ 0 \end{bmatrix} \end{cases} \tag{30}$$

$$\begin{cases} \mathbf{x_{EBM}}' = & \mathbf{A_{e2}} \mathbf{x_{EBM}} + \mathbf{B_{e2}} U_{\text{in}} \\ \mathbf{A_{e2}} = & \begin{bmatrix} -\frac{R_1}{2L_1} & -\frac{\omega_s M \cos(\alpha_2)}{2L_1} & 0 \\ \frac{\omega_s M \cos(\alpha_2)}{2L_2} & -\frac{R_2}{2L_2} & -\frac{S_2}{2L_2} \\ 0 & \frac{S_2}{2C_{fo}} & -\frac{1}{C_{fo} R_L} \end{bmatrix} \\ \mathbf{B_{e2}} = & \begin{bmatrix} \frac{S_1 \cos(\alpha_1)}{2L_1} \\ 0 \\ 0 \end{bmatrix}. \end{cases} \tag{31}$$

IV. Model Predictive Controller Design

MPC formulates an optimization problem based on a cost function. To evaluate the cost function at a certain control input, the dynamic model of the target system and the measurements of the state variables are required. By traversing the search space of the control signal, MPC can find the optimal control input minimizing the cost function at each control period. As the order of the system increases, the difficulties arises in computing the optimization loop and sampling the state variables. In IPT EV charging applications, the switching frequency ranges from 79–90 kHz, and the order of the ac-link is above four, which pose challenges to finish the optimization loop within one switching cycle. Simplifying the dynamic model becomes vital to facilitate the application of the MPC. To highlight the advantage of reducing the order of the dynamic model, MPC controllers are designed based on (24) and (31), respectively.

In both EBM and LPT methods, the state variables are derived from the first-order Fourier coefficient. As a discrete control strategy, the state variables have to be sampled at each control period. Considering the principle of phase shift control, the control period should be an integral multiple of the switching cycle T_s. In this section, the control period is set equal to T_s

$$\mathbf{A_{p4}} = \begin{bmatrix} -\frac{L_2 R_1}{F} & -\frac{L_2}{F} & \frac{M R_2}{F} & \frac{M}{F} & \omega_s & & & & -\frac{M \dot{S}_{2,r}}{F} \\ \frac{1}{C_1} & & & & & \omega_s & & & \\ \frac{M R_1}{F} & \frac{M}{F} & -\frac{L_1 R_2}{F} & -\frac{L_1}{F} & & & \omega_s & & \frac{L_1 \dot{S}_{2,r}}{F} \\ & & \frac{1}{C_2} & & & & & \omega_s & \\ -\omega_s & & & & -\frac{L_2 R_1}{F} & -\frac{L_2}{F} & \frac{M R_2}{F} & \frac{M}{F} & -\frac{M \dot{S}_{2,i}}{F} \\ & -\omega_s & & & \frac{1}{C_1} & & & & \\ & & -\omega_s & & \frac{M R_1}{F} & \frac{M}{F} & -\frac{L_1 R_2}{F} & -\frac{L_1}{F} & \frac{L_1 \dot{S}_{2,i}}{F} \\ & & & -\omega_s & & & \frac{1}{C_2} & & \\ & & -\frac{\dot{S}_{2,r}}{C_{fo}} & & & & -\frac{\dot{S}_{2,i}}{C_{fo}} & & -\frac{1}{R_L C_{fo}} \end{bmatrix} \tag{27}$$

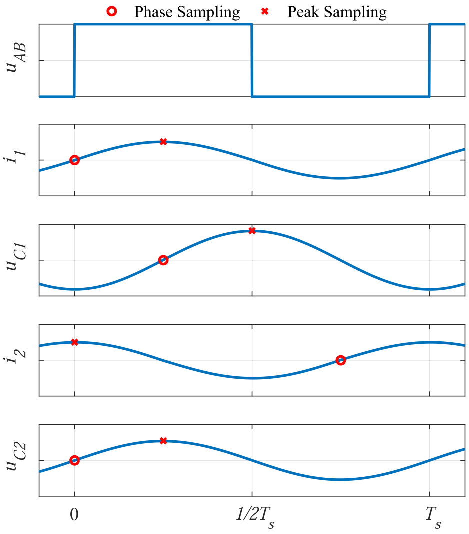

Fig. 8. Sampling sequence of the oscillating variables.

such that the control input can be updated at the start of each switching cycle. Based on the forward Euler method, the discrete predictive model can be obtained as (32). It should be noticed that the matrix $\mathbf{A_{p4}}$ is dependent on $\mathbf{x_{EBM}}(k)$ according to (20).

$$\begin{cases} \mathbf{x_{EBM}}(k+1) = (T_s\mathbf{A_{e1}} + \mathbf{I_{3\times3}})\mathbf{x_{EBM}}(k) + T_s\mathbf{B_{e1}}S_1U_{\text{in}} \\ \mathbf{x_{LPT}}(k+1) = (T_s\mathbf{A_{p4}}(k) + \mathbf{I_{9\times9}})\mathbf{x_{LPT}}(k) \\ \qquad\qquad + T_s\mathbf{B_{p2}}\begin{bmatrix} \dot{S}_{1,r}U_{\text{in}} \\ \dot{S}_{1,i}U_{\text{in}} \end{bmatrix}. \end{cases} \tag{32}$$

As shown in (32), the MPC based on the LPT method requires measurements of nine state variables. Regarding the measurements of the amplitude and phase of the oscillating variables, the sampling sequence is illustrated in Fig. 8, where u_{AB} is taken as the phase reference.

To control the power flow of the IPT system, u_{Cfo} is taken as the control target. However, the predictive models in (32) cannot convey an explicit function between the control input and the target. Thus, multiple iterations are required to obtain the response of u_{Cfo} under a certain θ. According to the matrix $\mathbf{B_{e1}}$ and $\mathbf{B_{p2}}$, the predictive models based on the EBM and LPT require three steps in each optimization loop. For example, at the k_{th} switching cycle, $U_{Cfo}(k+3)$ is calculated to compute the cost function for the MPC based on the EBM. In order to constrain the overshoot of i_1 and i_2, and to minimize the output ripple in the steady state, the cost functions are defined as

$$\begin{cases} G_{\text{EBM}} = & w_1\left|U^*_{Cfo} - U_{Cfo}(k+3)\right| + w_2\left|I^*_2 - I_2(k+2)\right| \\ & +w_3\left|I^*_1 - I_1(k+1)\right| \\ G_{\text{LPT}} = & w_4\left|U^*_{Cfo} - \sqrt{2}U_{Cfo}(k+3)\right| \\ & +w_5\left|I^*_2 - \sqrt{2}|\dot{I}_2(k+2)|\right| \\ & +w_6\left|I^*_1 - \sqrt{2}|\dot{I}_1(k+1)|\right| \end{cases} \tag{33}$$

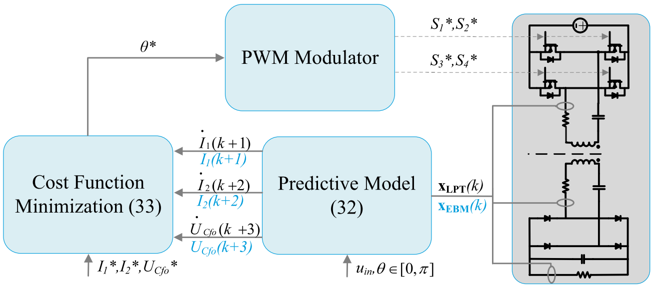

Fig. 9. Diagram of the proposed MPC controller.

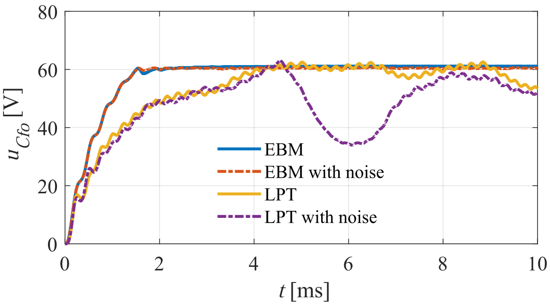

Fig. 10. Closed-loop transient response of the MPC controllers and impacts of the feedback noise, where $u_{\text{in}} = 100$ V, $U^*_{Cfo} = 60$ V, the circuit parameters are listed in Table I.

where w_1, w_2, w_3, w_4, w_5, and w_6 are the weight factors.

The structure of the MPC controllers is depicted in Fig. 9. Based on the measurements of the state variables, the predictions can be obtained by using (32). The predictions are evaluated by applying the cost functions in (33). The cost function minimization block can find the optimal control input θ^* under the current switching cycle. Although both the MPC controllers based on EBM and LPT methods execute three iterations for each given θ, the number of equations to be solved is three times larger in the controller based on the LPT strategy due to its high-order of the dynamic model. To finish the MPC optimization within one switching cycle, it is essential to reduce the computation labor, which makes the EBM more advantageous.

To compare the computation time of the developed MPC controllers, the optimization cycle is conducted in MATLAB on a computer with a Intel(R) Xeon(R) W-2123 CPU. In each optimization cycle, 50 different values of θ in the range of $[0, \pi]$ is assigned into the predictive model, whose results are compared according to the defined cost function. By conducting the optimization cycle 100 000 times, the average computation time of one optimization cycle is 0.0037 ms for the EBM and 1.6 ms for the LPT. This can prove that the MPC controller based on EBM is more practical to control IPT systems.

Fig. 10 presents the closed-loop transient response of the proposed MPC controllers. To investigate the impacts of the feedback measurement error, band-limited white noise (peak value less than 10% of the signal's steady state value, sampling frequency at 86.3 kHz) is added to the feedback signals. When the noise is absent, the MPC controllers using both the EBM and LPT methods can effectively regulate u_{Cfo}, while the MPC

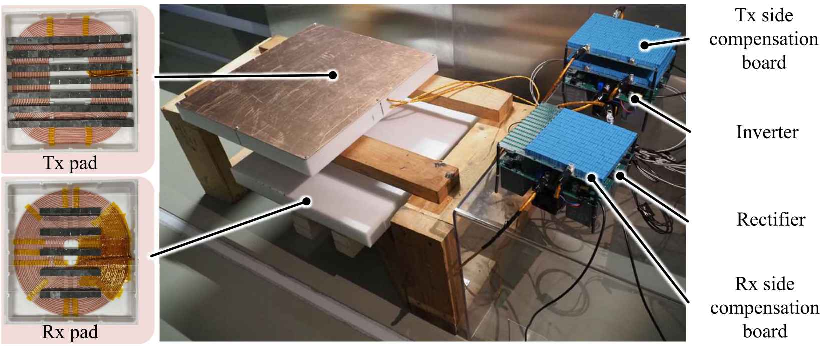

Fig. 11. Photograph of the IPT system.

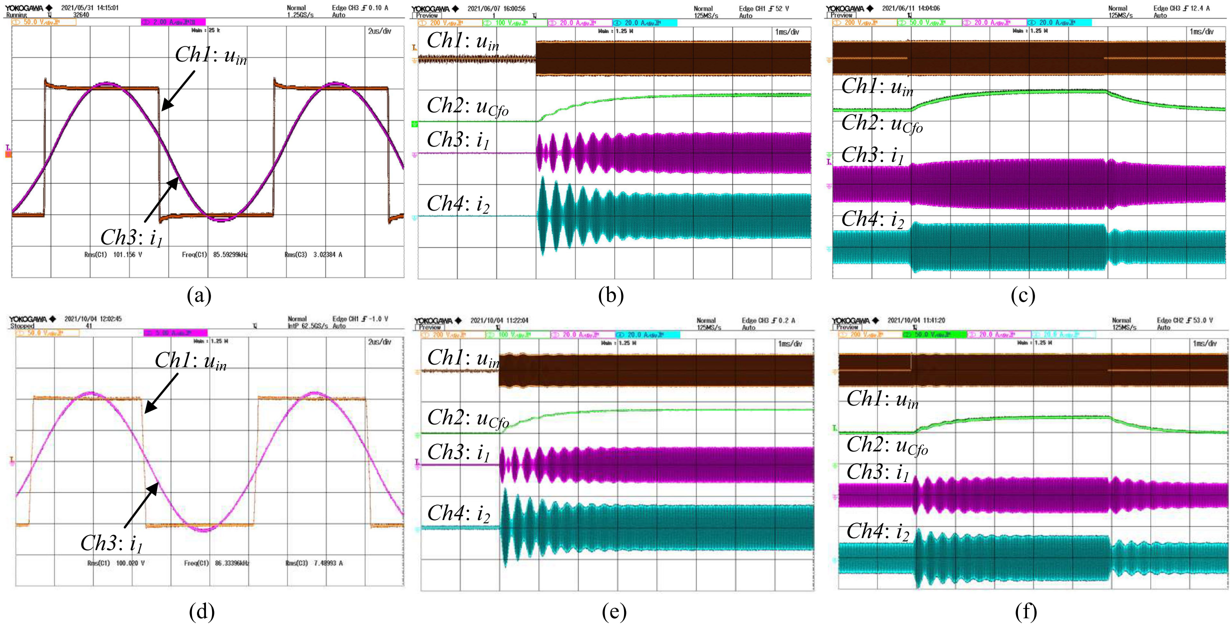

Fig. 12. Experimental waveforms for case A [(a)–(c)] and case B [(d)–(f)], (a) and (d) ZVS turn-ON operation of the H-bridge inverter; (b) and (e) start-up response of the IPT system; (c) and (f) step response starting from nonzero conditions.

controller based on the EBM strategy shows superiority in terms of the transient time, overshoot, and steady-state ripple. The waveform of the MPC controller based on the LPT method presents relatively large ripple, which mainly results from the error of measurements. As per Fig. 8, the sampling time of the phase and peak is not synchronized, and thus, there will be an error between the sampled values of the state variables and their real-values when the optimization starts running. Since there are eight state variables sampled from the oscillating waveform, the sampling error could accumulate on the predicted results. By contrast, the MPC controller based on the EBM requires two state variables from the waveform, which makes it more reliable. Moreover, peak sampling is easier to be realized in software or hardware than the phase sampling in practice. When the noise is added to the feedback signals, the MPC controller based on EBM delivers almost the same transient response, while the transient behaviors of the controller based on the LPT method have a longer transient time and a larger ripple.

V. EXPERIMENTAL VALIDATION

To verify the developed EBM and MPC controller, experiments are conducted in the IPT system shown in Fig. 11. Two cases (case A and case B) of experiments are conducted to show the accuracy of the proposed EBM under different switching frequencies. The experimental system parameters for these two cases are listed in Table I, where ω_s and the resonant frequency for the Tx $\omega_{r,1}$ and Rx $\omega_{r,2}$ sides are included. In both cases, the ZVS turn-ON operation of the H-bridge inverter is achieved. Compared with case A, case B operates closer to the natural resonance of the IPT system, and the EBM, thus, delivers a higher prediction accuracy for case B. u_{in} is set to be constant and equal to 100 V in all the experiments.

A. Start-Up Response

The start-up waveforms that are illustrated in Fig. 12(b) and (e) are measured when θ steps from zero to π. Fig. 12(a) and (d) shows that i_1 slightly lags u_{in} and the ZVS operation of the

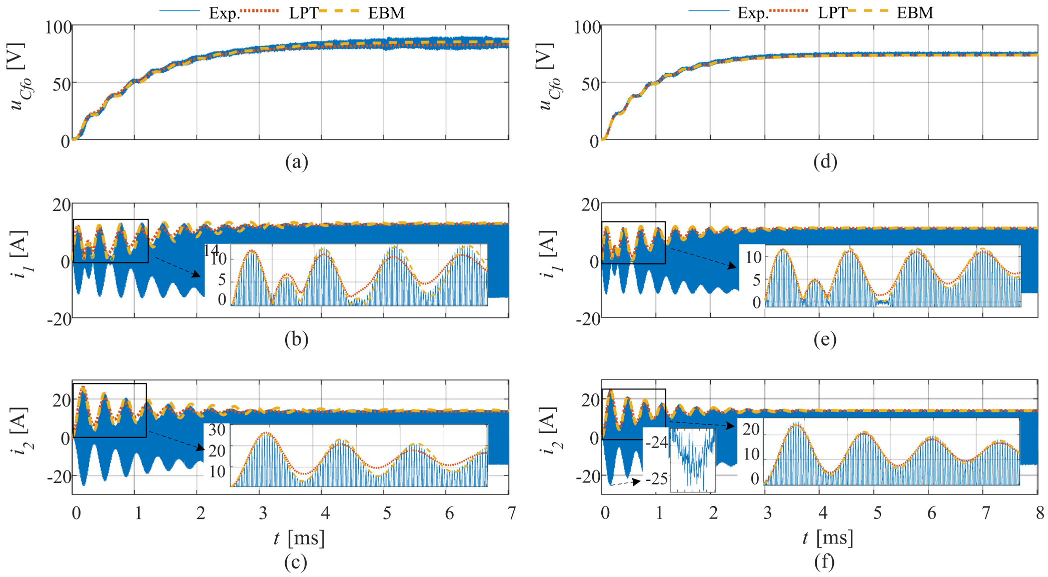

Fig. 13. Comparison of the start-up responses between the experimental results and the solutions derived from the analytical dynamic models for case A [(a)–(c)] and case B [(d)–(f)].

inverter is guaranteed. By applying the same conditions, u_{Cfo}, i_1, and i_2 predicted by the LPT in (24) and by the EBM in (31) are compared with the experimental results, as depicted in Fig. 13. Since $|\dot{I}_1|$ and $|\dot{I}_2|$ represent the rms value of i_1 and i_2 at the fundamental frequency in the LPT method, the curves from the LPT dynamic model indicates the value of $\sqrt{2}|\dot{I}_1|$ and $\sqrt{2}|\dot{I}_2|$.

In Fig. 13, a better agreement between the analytical and experimental results can be observed in case B because the operation frequency of case B is closer to the resonance than case A. In Fig. 13(a) and (d), the analytical models accurately predict the transients of u_{Cfo}. In Fig. 13(e) and (f), the ripples of the waveform envelop are accurately predicted by the EBM. Although the predicted curves shows a small error in the later stage of the transients in Fig. 13(b) and (c), the EBM can accurately predict the early stage of the step response as shown in the zoomed-in views, which ensures that the overshoot can be accurately estimated.

Both EBM and LPT models can mostly match the peaks of i_1 and i_2, and the EBM becomes more accurate when the IPT system operates closer to the its resonance point. It proves that the EBM can accurately predict the transients of the SS compensated IPT system starting from zero conditions.

B. Step Response Starting From Nonzero Conditions

To test the accuracy of the proposed EBM model, step responses under nonzero conditions are measured on the IPT system. When the system reaches steady state with θ equal to $\frac{\pi}{2}$, a step of $\frac{\pi}{2}$ is added to θ. After 5 ms, a step of $-\frac{\pi}{2}$ is added to θ. The measured waveforms are presented in Fig. 12(c) and (f). By applying the same operating conditions, the predicted curves from the EBM and LPT methods are compared with the measured waveforms in Fig. 14.

Similar to the step response, the prediction accuracy of case B is generally higher than case A because the operating frequency of case B is close to the resonant frequency of the IPT system. In Fig. 14(a) and (d), the analytical results of u_{Cfo} match the measurements well, which implies that the proposed EBM can be used to design controller for the output power regulation. In the prediction of i_1 and i_2 in case A, the EBM and LPT methods both overestimate the overshoot, and the curves from the EBM takes longer time to reach the steady state, as shown in Fig. 14(b) and (c). By contrast, the prediction accuracy in case B is obviously higher, and the curves of the EBM and the LPT method overlap mostly. Therefore, the EBM strategy is proved to be able to accurately predict the system transient responses starting from nonzero conditions.

C. Transient Response Using MPC Controllers

To prove the advantage of the presented EBM in reducing the order of the dynamic model, the MPC controllers are developed in Section IV. Since the main idea of this article is the proposed dynamic modeling method, the MPC controllers are not physically implemented on the IPT system. Instead of building the real feedback controller, a lookup table of the control input, generated from circuit simulations, is applied to control the IPT system. The circuit simulation model utilizes the same parameters of case B as listed in Table I. The reference voltage is set to be 60 V. The control input is obtained from simulations using MPC based on the EBM and LPT methods.

The experimental waveforms are illustrated in Fig. 15(a) and (b). The MPC based on the EBM can effectively regulate u_{Cfo}, while the MPC based on the LPT method shows an obvious ripples in u_{Cfo} and the envelops of the winding currents also oscillate. The experimental results are also compared with the simulations in Fig. 15(c) and (d). The simulated curves match the measurements well, which proves that the simulation models can accurately reflect the transients of the IPT system. In Fig. 15(c), the MPC based on the EBM delivers good dynamic

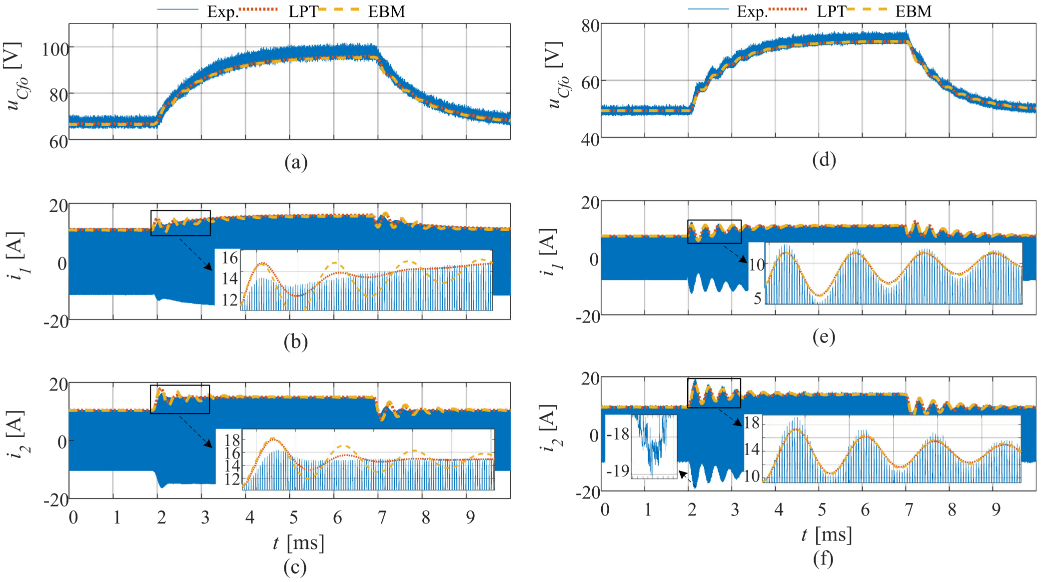

Fig. 14. Comparison of the step responses starting from nonzero conditions between the experimental results and the solutions derived from the analytical dynamic models for case A [(a)–(c)] and case B [(d)–(f)].

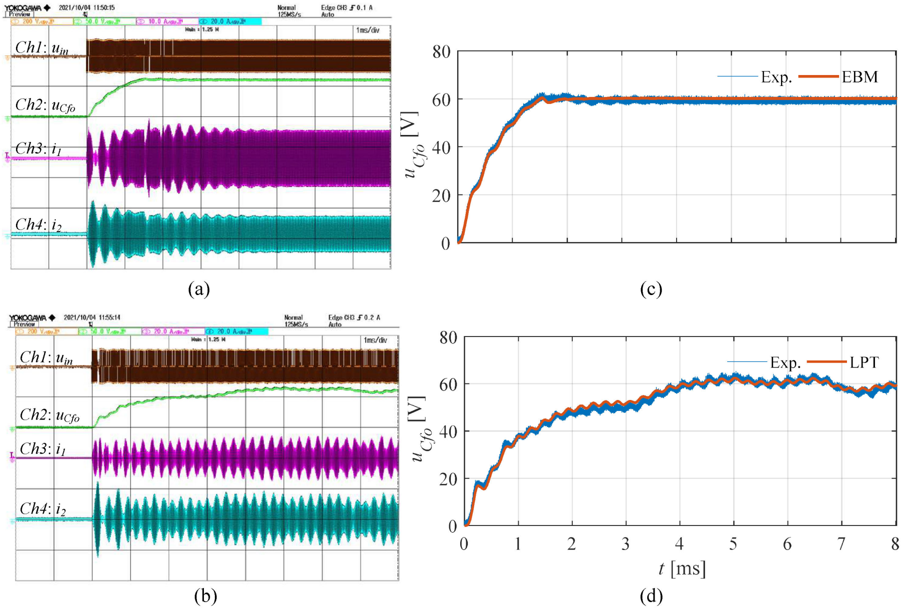

Fig. 15. Measured transient response using MPC methods based on (a) EBM and (b) LPT strategies. The comparison between the measurements and simulations are presented in (c) and (d).

performances. u_{Cfo} reaches steady state in 1.5 ms with almost no overshoot. By contrast, the transient time is longer and u_{Cfo} fluctuates in the steady state in Fig. 15(d). This is because the MPC based on LPT requires feedback signals of nine state variables. The sampling timing cannot be synchronized, as illustrated in Fig. 8, leading to errors in the feedback signals. As a result, the predicted results are inaccurate in each optimization cycle of the MPC controllers based on the LPT method. The developed MPC based on the EBM is proven to be effective in regulating the output voltage of the IPT system. Meanwhile, it is also an evidence that the proposed EBM can accurately model the dynamics of the IPT system.

VI. CONCLUSION

This article develops a dynamic modeling method for IPT systems based on the energy interactions between the resonant tanks. To verify the accuracy of the proposed EBM, the dynamic models of an SS compensated IPT system are built based on the EBM and LPT methods. By using the EBM, the dynamic model of the ac-link is of second-order, which is one fourth that of the LPT strategy. To prove the accuracy of the EBM when the switching frequency deviates from the resonant frequency, the transient behavior of the IPT system is studied in the switching frequency range of 85–87 kHz. To further show the advantage of the EBM, the EBM and LPT methods are applied to design MPC controllers. The MPC controller based on the EBM requires just three feedback signals and less computation time, and delivers a better transient response than the LPT strategy. Finally, experiments are conducted to validate the accuracy of the EBM and the effectiveness of the developed MPC controller based on the EBM.

In this article, a lookup table of the control input is used to regulate the IPT system. It is valuable to further investigate the impact of the sampling delay and computation time on the transient performance of the developed MPC controller. We will physically build an MPC controller to control the IPT system as our future work.

REFERENCES

[1] S. Cui, Z. Wang, S. Han, C. Zhu, and C. C. Chan, "Analysis and design of multiphase receiver with reduction of output fluctuation for EV dynamic wireless charging system," *IEEE Trans. Power Electron.*, vol. 34, no. 5, pp. 4112–4124, May 2019.

[2] S. Y. Jeong, J. H. Park, G. P. Hong, and C. T. Rim, "Autotuning control system by variation of self-inductance for dynamic wireless EV charging with small air gap," *IEEE Trans. Power Electron.*, vol. 34, no. 6, pp. 5165–5174, Jun. 2019.

[3] S. Zhou and C. C. Mi, "Multi-paralleled LCC reactive power compensation networks and their tuning method for electric vehicle dynamic wireless charging," *IEEE Trans. Ind. Electron.*, vol. 63, no. 10, pp. 6546–6556, Oct. 2016.

[4] N. Fu, J. Deng, Z. Wang, W. Wang, and S. Wang, "A hybrid mode control strategy for LCC-LCC compensated WPT system with wide ZVS operation," *IEEE Trans. Power Electron.*, vol. 37, no. 2, pp. 2449–2460, Feb. 2022.

[5] Z. Zhou, L. Zhang, Z. Liu, Q. Chen, R. Long, and H. Su, "Model predictive control for the receiving-side DC of dynamic wireless power transfer," *IEEE Trans. Power Electron.*, vol. 35, no. 9, pp. 8985–8997, Sep. 2020.

[6] W. Shi *et al.*, "Design of a highly efficient 20 kW inductive power transfer system with improved misalignment performance," *IEEE Trans. Transp. Electrific.*, to be published, doi: 10.1109/TTE.2021.3133759.

[7] J. M. Miller *et al.*, "Demonstrating dynamic wireless charging of an electric vehicle: The benefit of electrochemical capacitor smoothing," *IEEE Power Electron. Mag.*, vol. 1, no. 1, pp. 12–24, Mar. 2014.

[8] G. A. Covic, J. T. Boys, M. L. G. Kissin, and H. G. Lu, "A three-phase inductive power transfer system for roadway-powered vehicles," *IEEE Trans. Ind. Electron.*, vol. 54, no. 6, pp. 3370–3378, Dec. 2007.

[9] W. Shi, F. Grazian, S. Bandyopadhyay, J. Dong, T. B. Soeiro, and P. Bauer, "Analysis of dynamic charging performances of optimized inductive power transfer couplers," in *Proc. IEEE 19th Int. Power Electron. Motion Control Conf.*, 2021, pp. 751–756.

[10] C. Riekerk, "Digital control of a wireless power transfer system for electrical vehicles," M.Sc. thesis, TU Delft, Delft, The Netherlands, Jun. 2020. [Online]. Available: http://resolver.tudelft.nl/uuid:3aa0f0e5-96be-466d-9a0f-28fdb4c53813

[11] W. Shi, J. Deng, Z. Wang, and X. Cheng, "The start-up dynamic analysis and one cycle control-PD control combined strategy for primary-side controlled wireless power transfer system," *IEEE Access*, vol. 6, pp. 14439–14450, 2018.

[12] S. Bandyopadhyay, P. Venugopal, J. Dong, and P. Bauer, "Comparison of magnetic couplers for IPT-based EV charging using multi-objective optimization," *IEEE Trans. Veh. Technol.*, vol. 68, no. 6, pp. 5416–5429, Jun. 2019.

[13] T. Diekhans and R. W. D. Doncker, "A dual-side controlled inductive power transfer system optimized for large coupling factor variations and partial load," *IEEE Trans. Power Electron.*, vol. 30, no. 11, pp. 6320–6328, Nov. 2015.

[14] A. K. Swain, M. J. Neath, U. K. Madawala, and D. J. Thrimawithana, "A dynamic multivariable state-space model for bidirectional inductive power transfer systems," *IEEE Trans. Power Electron.*, vol. 27, no. 11, pp. 4772–4780, Nov. 2012.

[15] S. R. Sanders, J. M. Noworolski, X. Z. Liu, and G. C. Verghese, "Generalized averaging method for power conversion circuits," in *Proc. 21st Annu. IEEE Conf. Power Electron. Specialists*, 1990, pp. 333–340.

[16] H. Hao, G. A. Covic, and J. T. Boys, "An approximate dynamic model of LCL- T-based inductive power transfer power supplies," *IEEE Trans. Power Electron.*, vol. 29, no. 10, pp. 5554–5567, Oct. 2014.

[17] C. T. Rim and G. H. Cho, "Phasor transformation and its application to the DC/AC analyses of frequency phase-controlled series resonant converters (SRC)," *IEEE Trans. Power Electron.*, vol. 5, no. 2, pp. 201–211, Apr. 1990.

[18] S. Lee, B. Choi, and C. T. Rim, "Dynamics characterization of the inductive power transfer system for online electric vehicles by laplace phasor transform," *IEEE Trans. Power Electron.*, vol. 28, no. 12, pp. 5902–5909, Dec. 2013.

[19] H. Li, J. Fang, and Y. Tang, "Dynamic phasor-based reduced-order models of wireless power transfer systems," *IEEE Trans. Power Electron.*, vol. 34, no. 11, pp. 11361–11370, Nov. 2019.

[20] Z. U. Zahid *et al.*, "Modeling and control of series," *IEEE Trans. Emerg. Sel. Topics Power Electron.*, vol. 3, no. 1, pp. 111–123, Mar. 2015.

[21] H. A. Haus and W. Huang, "Coupled-mode theory," *Proc. IEEE*, vol. 79, no. 10, pp. 1505–1518, Oct. 1991.

[22] H. Li, K. Wang, L. Huang, W. Chen, and X. Yang, "Dynamic modeling based on coupled modes for wireless power transfer systems," *IEEE Trans. Power Electron.*, vol. 30, no. 11, pp. 6245–6253, Nov. 2015.

[23] J. Tang, S. Dong, C. Cui, and Q. Zhang, "Sampled-data modeling for wireless power transfer systems," *IEEE Trans. Power Electron.*, vol. 35, no. 3, pp. 3173–3182, Mar. 2020.

[24] A. Kurs, A. Karalis, R. Moffatt, J. D. Joannopoulos, P. Fisher, and M. Soljacic, "Wireless power transfer via strongly coupled magnetic resonances," *Science*, vol. 317, no. 5834, pp. 83–86, Jul. 2007.

[25] M. Kiani and M. Ghovanloo, "The circuit theory behind coupled-mode magnetic resonance-based wireless power transmission," *IEEE Trans. Circuits Syst. I, Reg. Papers*, vol. 59, no. 9, pp. 2065–2074, Sep. 2012.

[26] J. T. Boys, G. A. Covic, and Y. Xu, "DC analysis technique for inductive power transfer pick-ups," *IEEE Power Electron. Lett.*, vol. 1, no. 2, pp. 51–53, Jun. 2003.

[27] J. Xu *et al.*, "Carrier-based modulated model predictive control strategy for three-phase two-level VSIs," *IEEE Trans. Energy Convers.*, vol. 36, no. 3, pp. 1673–1687, Sep. 2021.

[28] C. Qi, Z. Lang, L. Su, X. Chen, and H. Miao, "Finite-control-set model predictive control for a wireless power transfer system," in *Proc. IEEE Int. Symp. Predictive Control Elect. Drives Power Electron.*, 2019, pp. 1–5.

[29] S. Li, W. Li, J. Deng, T. D. Nguyen, and C. C. Mi, "A double-sided LCC compensation network and its tuning method for wireless power transfer," *IEEE Trans. Veh. Technol.*, vol. 64, no. 6, pp. 2261–2273, Jun. 2015.

[30] Chwei-Sen Wang, G. A. Covic, and O. H. Stielau, "Power transfer capability and bifurcation phenomena of loosely coupled inductive power transfer systems," *IEEE Trans. Ind. Electron.*, vol. 51, no. 1, pp. 148–157, Feb. 2004.

[31] Y. Geng, Z. Yang, and F. Lin, "Design and control for catenary charged light rail vehicle based on wireless power transfer and hybrid energy storage system," *IEEE Trans. Power Electron.*, vol. 35, no. 8, pp. 7894–7903, Aug. 2020.

[32] W. V. Wang and D. J. Thrimawithana, "A novel converter topology for a primary-side controlled wireless EV charger with a wide operation range," *IEEE J. Emerg. Sel. Topics Ind. Electron.*, vol. 1, no. 1, pp. 36–45, Jul. 2020.

[33] R. Bosshard and J. W. Kolar, "Multi-objective optimization of 50 kW/85 kHz IPT system for public transport," *IEEE Trans. Emerg. Sel. Topics Power Electron.*, vol. 4, no. 4, pp. 1370–1382, Dec. 2016.

Wenli Shi (Graduate Student Member, IEEE) received the B.S. degree in automotive engineering from Jilin University, Changchun, China, in 2015, and the M.S. degree in mechanical engineering from the Beijing Insitiue of Technology, Beijing, China, in 2018. He is currently working toward the Ph.D. degree in the field of dynamic wireless charging of electric vehicles with the DC System, Energy Conversion and Storage (DCE&S) Group, Delft University of Technology, Delft, The Netherlands.

His research interests include foreign object detection, multiobjectives optimization design, dynamic modeling, and control for wireless power transfer.

Jianning Dong (Member, IEEE) received the B.S. and Ph.D. degrees in electrical engineering from Southeast University, Nanjing, China, in 2010 and 2015, respectively.

Since 2016, he has been an Assistant Professor with the DC System, Energy Conversion and Storage (DCE&S) Group, Delft University of Technology (TU Delft), Delft, The Netherlands. Before joining TU Delft, he was a Postdoctoral Researcher with McMaster Automotive Resource Centre, McMaster University, Hamilton, ON, Canada. His research interests include electromechanical energy conversion and contactless power transfer.

Thiago Batista Soeiro (Senior Member, IEEE) received the B.Sc.(Hons.) and M.Sc. degrees in electrical engineering from the Federal University of Santa Catarina, Florianopolis, Brazil, in 2004 and 2007, respectively, and the Ph.D. degree from the Swiss Federal Institute of Technology, Zurich, Switzerland, in 2012.

During the master's and Ph.D. studies, he was a Visiting Scholar with the Power Electronics and Energy Research Group, Concordia University, Montreal, QC, Canada, and with the Center for Power Electronics Systems, Blacksburg, VA, USA, respectively. From 2012 to 2013, he was a Researcher with Power Electronics Institute, Federal University of Santa Catarina. From October 2013 to April 2018, he worked initially as a Scientist and later as a Senior Scientist with Corporate Research Center, ABB Switzerland, Ltd., Baden-Dattwil, Switzerland. Since May 2018, he has been working with the DC Systems, Energy Conversion and Storage Group, Delft University of Technology, Delft, The Netherlands. In January 2022, he joined European Space Agency and is currently working as a Power Conditioning Engineer. His research interests include advanced high power converters and dc system integration.

Dr. Soeiro was a recipient of the 2013 IEEE Industrial Electronics Society Best Conference Paper Award and the Best Paper Awards in the following IEEE conferences: International Conference on Power Electronics (ECCE Asia 2011), International Conference on Industrial Technology (ICIT 2013), Conference on Power Electronics and Applications EPE'15 (ECCE Europe 2015), and 19th International Power Electronics and Motion Control Conference (PEMC 2020).

Junjun Deng (Member, IEEE) received the B.S., M.S., and Ph.D. degrees in electrical engineering from Northwestern Polytechnical University, Xi'an, China, in 2008, 2011, and 2015, respectively.

From 2011 to 2014, he was a Visiting Scholar with the Department of Electrical and Computer Engineer, University of Michigan, Dearborn. He is currently an Associate Professor with the School of Mechanical Engineering, Beijing Institute of Technology, Beijing, China. His research interests include wireless power transfer, resonant power conversion, and advanced battery chargers for electric vehicles.

Calvin Riekerk (Graduate Student Member, IEEE) received the B.S. and M.S. degrees in electrical engineering from the Delft University of Technology, TU Delft, The Netherlands, in 2018 and 2020, respectively. He is currently working toward the Ph.D. degree with the DC System, Energy Conversion and Storage (DCE&S) Group, TU Delft, The Netherlands.

His research interests include wireless power transfer.

Pavol Bauer (Senior Member, IEEE) received the master's degree in electrical engineering from the Technical University of Kosice, Kosice, Slovakia, in 1985, and the Ph.D. degree from the Delft University of Technology, Delft, The Netherlands, in 1995.

He is currently a Full Professor with the Department of Electrical Sustainable Energy, Delft University of Technology and the Head of DC Systems, Energy Conversion and Storage Group. He received the title Prof. from the President of Czech Republic with the Brno University of Technology, in 2008, and Delft University of Technology, in 2016. He is also the Honorary Professor with the Politehnica University Timisioira, Romania. From 2002 to 2003, he was working partially with KEMA (DNV GL, Arnhem) on different projects related to power electronics applications in power systems. He authored or coauthored more than 95 journal and 350 conference papers in his field (with H-factor Google scholar 39, Web of Science 29), he is an author or coauthor of 8 books, holds 9 international patents and organized several tutorials at the international conferences. He has worked on many projects for industry concerning wind and wave energy, power electronic applications for power systems, such as Smarttrafo; HVDC systems, projects for smart cities, such as PV charging of electric vehicles, PV and storage integration, contactless charging; and he participated in several Leonardo da Vinci, H2020 and Electric Mobility Europe EU projects as project partner (ELINA, INETELE, E-Pragmatic, Micact, Trolly 2.0, OSCD) and coordinator (PEMCWebLab.com-Edipe, SustEner, Eranet DCMICRO).

Dr. Bauer is a the Former Chairman of Benelux IEEE Joint Industry Applications Society, Power Electronics and Power Engineering Society chapter, Chairman of the Power Electronics and Motion Control (PEMC) council, member of the Executive Committee of European Power Electronics Association (EPE), and also a member of International Steering Committee at numerous conferences.